Available online at www.sciencedirect.com
SCIENCE DIRECT®
International Journal of Heat and Mass Transfer 48 (2005) 487–499
International Journal of HEAT and MASS TRANSFER
www.elsevier.com/locate/ijhmt

Energy transport and material removal in wide bandgap materials by a femtosecond laser pulse

L. Jiang, H.L. Tsai *

Laser-Based Manufacturing Laboratory, Department of Mechanical and Aerospace Engineering, Mechanical Engineering Building, University of Missouri–Rolla, 1870 Miner Circle, Rolla, MO 65409 1350, United States

Received 26 February 2004; received in revised form 10 September 2004
Available online 6 November 2004

Abstract

A new model is proposed which greatly improves the accuracy in predicting the ablation depth and, for the first time, can predict the flat-bottom crater shape for wide bandgap materials ablated by a femtosecond laser pulse. The model calculates the transient distributions of free electron density and free electron temperature. The quantum treatment is employed to account for the specific heat and the relaxation time for free electrons. The temporal and spatial dependent optical properties of the dense plasma are considered. The predicted threshold fluence and ablation depth for fused silica are in agreement with published experimental data.

1. Introduction

There is no rigorous definition of wide bandgap materials. Wide bandgap materials are usually referred to as materials with a bandgap greater than 3 eV including dielectrics and some semiconductors and are considered to be difficult for laser processing. Femtosecond laser ablation of wide bandgap materials is an active research area which has very significant scientific and engineering merits [1–4]. In the ablation process, materials are first transformed into absorbing plasma with metallic properties and, then, the subsequent laser–plasma interaction causes material removals [5–8]. Energy transport in the ablation process can be divided into two stages: (1) the photon energy absorption, mainly through free electron generation and heating, and (2) the redistribution of the absorbed energy to lattice leading to material removals [8,9]. This stage separation is based on the assumption that free electron generation and heating are completed in such a short time that the lattice temperature remains unchanged during the duration of a femtosecond laser pulse [10]. In femtosecond laser ablation, the classical heat transfer theories fail to describe the energy and mass transport in the nanometer length scale and femtosecond time scale, especially the dissipation of the absorbed energy to lattice and the corresponding material removal process [11–15]. Several material removal mechanisms, such as the Coulomb explosion and nonequilibrium thermal vaporization, may coexist and change from one mechanism to another during the removal process [14].

Comparing with the mechanisms of material removal, the phenomena of free electron generation and heating are much better understood [16]. At laser intensities on the order of 10^{13} to 10^{14} W/cm^2 impact ionization (mainly avalanche ionization) and photoionization (mainly multiphoton ionization) are the two major competing

* Corresponding author. Tel.: +1 573 341 4945; fax: +1 573 341 4115.
E-mail address: tsai@umr.edu (H.L. Tsai).

0017-9310/$ - see front matter © 2004 Elsevier Ltd. All rights reserved.
doi:10.1016/j.ijheatmasstransfer.2004.09.016

Nomenclature

a_i	impact ionization constant
b_{max}	maximum collision parameter, Eq. (20)
b_{min}	minimum collision parameter, Eq. (20)
c	scalar speed of light in vacuum
$\mathbf{c}$	vector velocity of light in vacuum
c_e	average specific heat per electron
c_M	electron specific heat per mole
d	crater depth
e	electron charge
$\mathbf{f}$	complex refractive index
f_1	normal refractive index
f_2	extinction coefficient
F	laser fluence
F_{th}	threshold fluence
h	Planck's constant
$\hbar$	reduced Planck's constant
I	laser intensity
I_0	peak laser intensity
k_B	Boltzmann's constant
m_e	nonrelativistic mass of electron
M	atomic mass unit
n_{cr}	critical free electron density
n_e	free electron density
$\langle n_k \rangle$	average number of electrons in energy state ε_k
N	number of photons required in photoionization
N_A	Avogadro's constant
N_e	total number of free electrons
P	photoionization term in Eq. (1)
r	distance to the Gaussian beam axis
r_0	radius of laser beam
R	reflectivity
t	time
t_p	pulse duration
T	free electron temperature in Kelvin
T_D	Debye temperature
T_F	Fermi temperature
T_l	lattice temperature
T_{ev}	average kinetic energy of free electrons in eV
U_I	ionization potential
$\mathbf{v}$	velocity of light in material
z	depth from surface in bulk material
Z	charge state of ions

Greek symbols

α	absorption coefficient of free electrons
α_h	absorption coefficient via electron heating
$\rho(\varepsilon)$	the density of states, Eq. (28)
β	impact ionization term in Eq. (1)
δ_N	cross-section of N-photon ionization
ε_F	Fermi energy
ε_k	energy state
$\boldsymbol{\epsilon}$	complex dielectric function
$\langle \varepsilon \rangle$	average electron kinetic energy
ϵ_0	electrical permittivity of free space
ϵ_1	real component of dielectric function
ϵ_2	imaginary component of dielectric function
γ	electron heat capacity constant
λ	laser wavelength
$\ln \Lambda$	Coulomb logarithm, Eq. (19)
μ	chemical potential
ν_e	electron collision frequency
ν_{ei}	electron–ion collision frequency
ν_{ep}	electron–phonon collision frequency
ω	laser frequency
ω_p	plasma frequency
τ_e	free electron relaxation time

mechanisms for free electron generation [17,18]. A well-recognized theory, flux-doubling model, was developed based on the Fokker–Planck equation by employing the following two assumptions: (1) as soon as the kinetic energy of an electron reaches the critical energy, it produces another electron, and both the electrons become zero kinetic energy and (2) the shape of electron distribution remains unchanged during the impact ionization process. The model was validated by experiments in the femtosecond laser ablation of dielectrics [17–23].

However, so far the free electron heating is not properly addressed. To study free electron heating, the laser-induced electrical field inside the material must be determined which can be found as a solution to the Maxwell equation. The solution is straightforward when the optical properties of ablation material are assumed to be constant in time and space and independent of the incident laser intensity. With these assumptions, the free electron heating falls into the framework of the well-known skin-effect model. However, the optical properties of the ionized material are actually time, space, and laser intensity dependent under a femtosecond laser pulse, and they turn out to be critical for determining the ablation crater shape [24]. Also, the flux-doubling model and the skin-effect model do not consider quantum effects that are significant for the dense plasma generated by a femtosecond laser pulse [11].

Using free electron density as the basic quantity, this study proposes a new mathematical model to predict the

threshold fluence and crater shape in the femtosecond laser ablation of wide bandgap materials at the laser peak intensities on the order of 10^{13} to 10^{14} W cm^2. The flux-doubling model in two-dimensional form is employed to investigate the free electron generation. The free electron model for the plasma of metals and doped semiconductors is modified to determine the optical properties of the highly ionized wide bandgap materials. Quantum treatment is included to calculate the free electron specific heat, free electron temperature, and the free electron relaxation time. The fused silica (SiO_2) is used as an example to demonstrate and validate the proposed model.

2. Mathematical model

2.1. Free electron generation: ionization

Building up the density of free electrons is necessary in order to initialize laser ablation of wide bandgap materials. For materials ablated by femtosecond lasers, critical density is defined as the free electron density at which the plasma oscillation frequency is equal to the laser frequency. It is widely assumed that the ablation starts when the free electron density reaches the critical density [19–21,25,26]. Once the critical density is created, the originally transparent or semitransparent material becomes opaque, and a large percentage of the absorbed laser energy is deposited in a very thin surface layer within a short period of time, leading to the ablation of the thin layer. Hence, the threshold fluence can be assumed as the minimal fluence that just creates the critical density. Similarly, ablation depth is considered to be the maximum depth at which the free electron density is equal to the critical density. These assumptions make it possible to theoretically predict threshold fluence and ablation depth based on the distribution of free electron density without considering the subsequent phase change mechanisms. Assuming a Gaussian laser beam irradiating on a wide bandgap material, the following well-known equation based on the flux-doubling model and derived from the Fokker–Planck equation can be used to calculate the free electron generation [18,19,26]:

$$\frac{\partial n_e(t,r,z)}{\partial t} = \beta(I) n_e(t,r,z) + P(I) \tag{1}$$

where t is the time; r is the distance to the Gaussian beam axis, i.e., the radius perpendicular to the Gaussian beam axis; z is the depth from the surface of the bulk material; $n_e(t,r,z)$ is the free electron density; $\beta(I)$ is the impact ionization term; $P(I)$ is the photoionization term; and I is the laser intensity inside the bulk material which is a function of t, r, and z. Note possible free electron diffusion and recombination are not considered in Eq. (1) which has been proved to be a reasonable simplification under a femtosecond ablation [18,20,26]. The major issue for Eq. (1) is to determine the impact ionization term and the photoionization term. Stuart et al. [20] assumed the impact ionization is linearly proportional to the laser intensity as follows:

$$\beta(I) = a_i I(t,r,z) \tag{2}$$

where a_i is a constant, which is $4 \pm 0.6\,\text{cm}^2/\text{J}$ for fused silica [2]. The photoionization rate can be expressed as a function of laser intensity by [20]:

$$P(I) = \delta_N (I(t,r,z))^N \tag{3}$$

where δ_N is the cross-section of N-photon absorption. For fused silica (bandgap = 9 eV) and the laser wavelength of 780 nm used in the present study, six photons are required to free a bound electron and, hence, $\delta_6 = 6 \times 10^{8\pm0.9}\,\text{cm}^{-3}\,\text{ps}^{-1}(\text{cm}^2/\text{TW})^6$ [2].

The original laser beam before it interacts with the material is assumed to be a Gaussian distribution in time and space. It is also assumed that the laser focus point is at the material surface, $z = 0$. At the surface, the laser beam, partially reflected by the material, is described by

$$I(t,r,0) = I_0(1 - R(t,r)) \exp\left(-\frac{r^2}{r_0^2} - (4\ln 2)\left(\frac{t}{t_p}\right)^2\right) \tag{4}$$

where $R(t,r)$ is the reflectivity at $z = 0$; r_0 is the radius of the laser beam; t_p is the pulse duration; and I_0 is the peak intensity given by

$$I_0 = \frac{2F}{\sqrt{\pi/\ln 2}\, t_p} \tag{5}$$

where F is the laser fluence. At a point inside the bulk material, the change of laser intensity can be expressed by

$$\frac{\partial I(t,r,z)}{\partial z} = -\alpha(t,r,z) I(t,r,z) \tag{6}$$

where $\alpha(t,r,z)$ is the absorption coefficient of the material. Hence, the laser intensity inside the bulk materials is found to be:

$$I(t,r,z) = \frac{2F}{\sqrt{\pi/\ln 2}\, t_p}(1 - R(t,r)) \times \exp\left(-\frac{r^2}{r_0^2} - (4\ln 2)\left(\frac{t}{t_p}\right)^2 - \int_0^z \alpha(t,r,z)\,dz\right) \tag{7}$$

It is assumed the laser beam impinges perpendicularly to the material surface, and the refraction due to the presence of plasma is neglected in the present study. It is seen that the laser intensity can be determined if the time and space dependent reflectivity and absorption coefficient are obtained. Note the reflection of the laser energy is assumed to occur only at the surface, while the absorption of laser energy can occur within the material.

2.2. Laser–plasma interaction: optical properties

Using a full Boltzmann collision integral, Rethfeld et al. [27] have demonstrated that the absorption of femtosecond laser energy in a highly ionized wide bandgap material can be well described by laser–plasma interactions. This is due to the strong metallic properties of the ionized materials whose free electron density under a femtosecond pulse can be reached to 10^{21} to 10^{23} cm^{-3} that is comparable to those of metals [21,24]. Hence, in this study, the free electron model for the plasma of metals and doped semiconductors is used to determine the optical properties of the ionized wide bandgap materials. The spatial and temporal dependent of the complex dielectric function for the plasma is expressed as [28]

$$\epsilon(t,r,z) = 1 + \left(\frac{n_e(t,r,z)e^2}{m_e\epsilon_0}\right)\left(\frac{-\tau_e^2(t,r,z) + i\tau_e(t,r,z)/\omega}{1+\omega^2\tau_e^2(t,r,z)}\right) \tag{8}$$

where e is the electron charge; m_e is the mass of electron; ϵ_0 is the electrical permittivity of free space; ω is the laser frequency; and $\tau_e(t,r,z)$ is the free electron relaxation time. The plasma frequency is defined by [28]

$$\omega_p(n_e) = \sqrt{\frac{n_e(t,r,z)e^2}{m_e\epsilon_0}} \tag{9}$$

At the critical electron density, n_{cr}, the plasma frequency is equal to the laser frequency. Hence,

$$n_{cr} = \frac{4\pi^2c^2m_e\epsilon_0}{\lambda^2e^2} \tag{10}$$

where c is the scalar speed of light in vacuum and λ is the wavelength of the laser. Note in electrostatic unit (esu), $n_{cr} = \frac{\pi m_e c^2}{\lambda^2 e^2}$, which is consistent with that reported in Ref. [20]. The complex dielectric function can be split into the real and imaginary components as follows:

$$\begin{aligned}\boldsymbol{\epsilon}(t,r,z) &= \epsilon_1(t,r,z) + i\epsilon_2(t,r,z)\\ &= \left(1 - \frac{\omega_p^2(n_e)\tau_e^2(t,r,z)}{1+\omega^2\tau_e^2(t,r,z)}\right)\\ &\quad + i\left(\frac{\omega_p^2(n_e)\tau_e(t,r,z)}{\omega\left(1+\omega^2\tau_e^2(t,r,z)\right)}\right)\end{aligned} \tag{11}$$

The relationship between the complex refractive index, **f**, and the complex dielectric function is given by

$$\left(\frac{\mathbf{c}}{\mathbf{v}}\right) = \mathbf{f} = (f_1 + if_2) = \sqrt{\boldsymbol{\epsilon}} = \sqrt{\epsilon_1 + i\epsilon_2} \tag{12}$$

where **c** is the velocity of light in vacuum; **v** is the velocity of light in the material; f_1 is the normal refractive index; and f_2 is the extinction coefficient. Thus, the f_1 and f_2 functions can be derived as:

$$f_1(t,r,z) = \sqrt{\frac{\epsilon_1(t,r,z) + \sqrt{\epsilon_1^2(t,r,z) + \epsilon_2^2(t,r,z)}}{2}} \tag{13}$$

$$f_2(t,r,z) = \sqrt{\frac{-\epsilon_1(t,r,z) + \sqrt{\epsilon_1^2(t,r,z) + \epsilon_2^2(t,r,z)}}{2}} \tag{14}$$

The reflectivity of the ionized material is determined by the following Fresnel expression at the surface $z = 0$:

$$R(t,r) = \frac{(f_1(t,r,0)-1)^2 + f_2^2(t,r,0)}{(f_1(t,r,0)+1)^2 + f_2^2(t,r,0)} \tag{15}$$

The absorption coefficient of laser intensity by the plasma via the free electron heating is calculated by

$$\alpha_h(t,r,z) = \frac{2\omega f_2(t,r,z)}{c} \tag{16}$$

Note Eq. (16) represents only a part of the laser energy that is absorbed via free electron heating, and there is another part of absorption that is via ionization. For the femtosecond laser ablation of dielectrics, the total laser energy absorption coefficient including free electron heating and ionization is expressed by [20]:

$$\alpha(t,r,z) = \alpha_h(t,r,z) + a_i n_e(t,r,z)U_I \tag{17}$$

where U_I is the bandgap of material which is 9.0 eV for fused silica and a_i is the impact ionization constant as given in Eq. (2). Eq. (17) developed in Ref. [20] neglects the photoionization, which is a reasonable assumption when the contribution of the impact ionization to the final free electron density is much greater than that of the photoionization. This is true in the present study, to be justified later. Note the absorption coefficient inside the bulk material is only a function of the extinction coefficient and is independent of the normal refractive index. As shown in Eq. (15) and Eq. (17), if the free electron relaxation time is obtained, the optical properties of the ionized material can be determined.

2.3. Free electron heating: electron relaxation time

Generally, under a femtosecond laser pulse, free electrons can be excited by photons to very high average kinetic energies (temperatures) that are much higher than the Fermi energy (Fermi temperature). For free electrons at very high temperatures or low densities, they can be treated as an ideal gas and the free electron relaxation time, dominated by the electron–ion collisions, can be calculated by the following Spitzer formula [29,30]:

$$\tau_e(t,r,z) = \frac{1}{\nu_{ei}} = \frac{1}{3\times10^{-6}\ln\Lambda}\left(\frac{T_{ev}^{3/2}(t,r,z)}{n_e(t,r,z)Z}\right) \tag{18}$$

where ν_{ei} is the electron–ion collision frequency; Z is the charge state of ions; T_{ev} is the average kinetic energy in eV that is often used to represent the electron tempera-

ture in microscopic thermodynamics; and ln Λ is the Coulomb logarithm determined by [31]:

$$\ln \Lambda = \frac{1}{2} \ln \left(1 + \left(\frac{b_{\max}}{b_{\min}} \right)^2 \right) \tag{19}$$

where the maximum ($b_{\max}$) and minimum ($b_{\min}$) collision parameters are given by

$$b_{\max} = \frac{(k_B T/m_e)^{1/2}}{\max(\omega, \omega_p)}; \quad b_{\min} = \max \left(\frac{Ze^2}{k_B T}, \frac{\hbar}{(m_e k_B T)^{1/2}} \right) \tag{20}$$

where k_B is the Boltzmann's constant.

However, at the very beginning of laser ablation, the electron kinetic energy is relatively low, contributions to the free electron relaxation time from electron–phonon collisions could be important. Hence, in this study when the electron kinetic energy is lower than or comparable to the Fermi energy, both the contributions of electron–phonon and electron–ion collisions are considered, and the free electron relaxation time is determined by [32]:

$$\tau_e = \frac{1}{\nu_e} = \frac{1}{\nu_{ei} + \nu_{ep}} \tag{21}$$

where ν_e is the electron collision frequency and ν_{ep} is the electron–phonon collision frequency determined by [29,31]:

$$\frac{1}{\nu_{ep}} = \left(\frac{M}{m_e} \right)^{1/2} \frac{\hbar}{U_{IP}} \frac{T_D}{T_l} \left(\frac{n_e(t,r,z)}{n_{cr}} \right)^{1/3} \tag{22}$$

where M is the atomic mass unit; $\hbar = h/2\pi$ is the reduced Planck's constant (h is the Planck's constant); U_{IP} is the ionization potential that is 13.6 eV for fused silica [24]; T_D is the Debye temperature (290 K for fused silica); and T_l is the lattice temperature in K that is assumed to be a constant (300 K, room temperature) during the laser pulse duration.

As discussed previously, the free electron generation and heating are completed in a very short period of time during which the lattice temperature remains unchanged. The electron heating is governed by the following equation [24]:

$$c_e(T, n_e) n_e(t,r,z) \frac{\partial T(t,r,z)}{\partial t} = \alpha_h(t,r,z) I(t,r,z) \tag{23}$$

where T is the electron temperature; c_e is the specific heat of free electrons; and α_h is the free electron absorption coefficient given in Eq. (16). In a wide range of temperatures, the quantum treatment should be included to calculate the specific heat and to link T_{ev} and T for high-density free electrons. The average number of electrons, $\langle n_k \rangle$, in energy state ε_k in the Fermi–Dirac distribution is given by

$$\langle n_k \rangle = \frac{1}{e^{\beta(T)(\varepsilon_k - \mu(n_e,T))} + 1} \tag{24}$$

where $\beta(T) = 1/k_B T(t,r,z)$ and μ is the chemical potential. For free electron gas, the chemical potential can be calculated by [33]:

$$\mu(n_e, T) = \varepsilon_F(n_e) \left[1 - \frac{1}{3} \left(\frac{\pi k_B T(t,r,z)}{2\varepsilon_F(n_e)} \right)^2 \right] \tag{25}$$

where the higher order terms are neglected and ε_F is the Fermi energy that is determined by [34]:

$$\varepsilon_F(n_e) = \left(\frac{(hc)^2}{8 m_e c^2} \right) \left(\frac{3}{\pi} \right)^{2/3} (n_e(t,r,z))^{2/3} \tag{26}$$

Note the Fermi temperature, T_F, is defined by the relation: $k_B T_F = \varepsilon_F$. The average kinetic energy per electron in J, $\langle \varepsilon \rangle$, is calculated by

$$\langle \varepsilon \rangle = \frac{\sum_k \langle n_k \rangle \varepsilon_k}{N_e} = \frac{\int_0^\infty \frac{1}{e^{\beta(T)(\varepsilon - \mu(n_e,T))} + 1} \rho(\varepsilon) \varepsilon \, d\varepsilon}{\int_0^\infty \frac{1}{e^{\beta(T)(\varepsilon - \mu(n_e,T))} + 1} \rho(\varepsilon) \, d\varepsilon} \tag{27}$$

where ε is the kinetic energy of a free electron; N_e is the total number of free electrons; and $\rho(\varepsilon)$ is the density of states. Note $\langle \varepsilon \rangle$is a function of T and n_e, and the average kinetic energy per electron in the unit of eV, T_{ev}, can be obtained by dividing $\langle \varepsilon \rangle$by a conversion factor ($1\,\text{eV} = 1.602 \times 10^{-19}\,\text{J}$). The density of states for nonrelativistic free electrons is expressed by [34]:

$$\rho(\varepsilon) = \frac{8\sqrt{2}\pi m_e^{3/2}}{h^3} \sqrt{\varepsilon} \tag{28}$$

The average specific heat per free electron can be determined by the following definition of heat capacity:

$$c_e(T, n_e) = \left(\frac{\partial \langle \varepsilon \rangle}{\partial T} \right)_V \tag{29}$$

where V is the volume. Eq. (29) defines the relationship between T_{ev} (in eV) and T (in K) for free electrons. Note at temperatures much lower than the Fermi temperature, the average specific heat per free electron is given by [33]:

$$c_e = \frac{\pi^2}{2} \left(\frac{k_B T}{\varepsilon_F} \right) k_B = \gamma T \tag{30}$$

where γ is the electron heat capacity constant for a free electron. For comparison purpose, the average kinetic energy and specific heat for an ideal free electron gas in classical approach are given below:

$$\langle \varepsilon \rangle = \frac{3}{2} k_B T; \quad c_e = \frac{3}{2} k_B \tag{31}$$

2.4. Numerical procedure

The free electron densities, electron temperatures, optical properties, and thermal properties are calculated

as functions of time and space by the following iterative scheme: (a) calculate the distribution of free electron densities by solving Eq. (1) and using the most recent laser intensity, Eq. (7); (b) calculate the distribution of electron temperature by solving Eq. (23) using the most recent free electron specific heat, electron densities, absorption coefficient, and laser intensity; (c) update the average kinetic energy per free electron, free electron specific heat, and free electron relaxation time; (d) update the dielectric function, reflectivity and absorption coefficient; (e) update the laser intensity distribution; (f) repeat step a through step e until both the free electron density and electron temperature are converged; (g) advance to the next time step, back to step a and continue the iterative scheme until the end of the pulse duration. A small volume of material is ablated if its free electron density at the end of laser irradiation is greater than or equal to the critical density.

3. Results and discussion

Fig. 1(a) demonstrates the significant differences in free electron average kinetic energy between the quantum treatment using Eqs. (24)–(28) and the classical approach using Eq. (31) for temperatures lower than or comparable to the Fermi temperature at electron density $4.0\times10^{21}\,\mathrm{cm}^{-3}$. At this electron density, the Fermi energy is 0.92 eV and the corresponding Fermi temperature is $1.07\times10^{4}\,\mathrm{K}$. Fig. 1(b) shows the differences between the classical approach by Eq. (31), the approximation by Eq. (30), and the quantum treatment by Eqs. (24)–(29) for electron specific heat per mole, $c_M = N_A c_e$, where N_A is the Avogadro's constant. Note at very high free electron temperatures, both the average kinetic energy and the molar specific heat merge to the classical approach that considers free electrons as an ideal gas. On the other hand, as shown in Fig. 1(b), at low temperatures, the numerical results by quantum treatment overlap with the approximation. This implies that Eq. (30) can be simplified from Eqs. (24)–(29) at low temperatures. Fig. 1 clearly shows the necessity of quantum treatment for free electrons in femtosecond laser ablation. The importance of quantum effects is detailed in a comparison study on femtosecond laser damage of metal thin films using the classical two-temperature model and the improved two-temperature model with quantum treatments [35].

In this study, a $\lambda = 780\,\mathrm{nm}$ laser with $t_p = 50\,\mathrm{fs}$ and $r_0 = 50\,\mu\mathrm{m}$ Gaussian beam profile is used for the ablation of fused silica, and the calculated results are compared with experimental measurements to validate the proposed model. The experimental ablation threshold fluence is about $3.3\,\mathrm{J/cm^2}$, and the corresponding experimental ablation depth at $5\,\mathrm{J/cm^2}$ is about 200 nm [2]. The proposed model gives the results of $3.15\,\mathrm{J/cm^2}$ and 195 nm, respectively, for the threshold fluence and ablation depth.

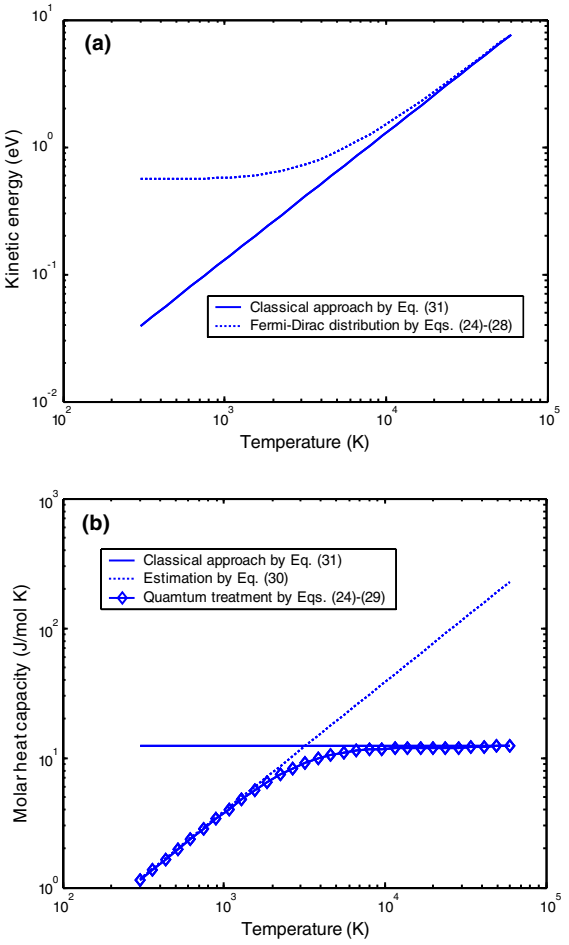

Fig. 1. The differences between different treatments for free electron density at $4.0\times10^{21}\,\mathrm{cm}^{-3}$ for (a) average free electron kinetic energy in eV and (b) molar free electron specific heat.

Fig. 2 shows the free electron density as a function of the ablation time at $r = 0$ and $z = 1\,\mathrm{nm}$ (the first grid layer in numerical calculations) for cases when only photoionization is considered and when both the impact ionization and photoionization are included. It is seen the free electron densities increase rapidly in the first few femtoseconds and then gradually increase until about 25 fs to reach the nearly "steady states." The photoionization dominates the free electron generation during the initial ionization process in about the first 5 fs until the free electron density reaches about 2.5×10 $17\,\mathrm{cm}^{-3}$ However, the contribution of impact ionization to the final free electron density is about $4.0\times10^{21}\,\mathrm{cm}^{-3}$ that is about two orders of magnitude greater than that of photoionization, $3.2\times10^{19}\,\mathrm{cm}^{-3}$ Hence, the neglect of multiphoton ionization in Eq. (17), as discussed earlier,

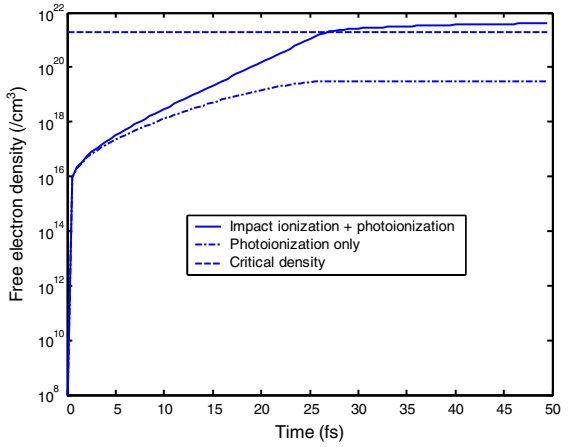

Fig. 2. The free electron density as a function of time; $r = 0$, $z = 1\,\text{nm}$, $t_p = 50\,\text{fs}$, $F = 5\,\text{J/cm}^2$.

is justified. The critical density, $1.8 \times 10^{21}\,\text{cm}^{-3}$ is achieved at about 27 fs. During the early stage of laser irradiation, 25 fs before the laser peak intensity, the contribution of six-photoionization to free electron density is smaller than $(1/2)^6$ of that of the peak intensity and thus the absorption coefficient is very small. During the later stage, 25 fs after the peak intensity, the reflectivity is very high and thus the free electron generation is limited. Hence, in this example, the calculation for the impact domain starts at 25 fs before the peak laser intensity and ends 25 fs after the peak laser intensity. The time step size of the numerical calculation is 0.5 fs.

Fig. 3 shows the reflectivity and absorption coefficient as a function of time at $r = 0$ and $z = 1\,\text{nm}$. It is seen that both the reflectivity and absorption coefficient are nearly zero at the initial stage of laser irradiation and increase drastically when the critical density is reached. From 23 fs to 30 fs, the reflectivity increases rapidly from nearly 0 to about 0.87. Hence, the laser energy after the formation of critical free electron density is mainly reflected. During the same period of time, the absorption coefficient also increases drastically from 146 to 6.9×10^4 cm. It is interesting to see that after 30 fs, the reflectivity remains almost constant, while the absorption coefficient continues to increase nearly linearly as a function of the ablation time. In this period, the free electron generation is dominated by the impact ionization through the collisions of highly excited free electrons, which has more influence on absorption coefficient, as shown in Eq. (17), than on the reflectivity after the creation of the critical density. After the formation of critical density, although only a small fraction of the laser energy is absorbed, the absorbed laser energy is mainly deposited in a very thin layer which leads to the material ablation. The result is consistent with the previous assumption that the ablation starts when the electron density reaches the critical density.

The laser intensity distributions in time domain and at $r = 0$ and different depths in the material are shown in Fig. 4. In 0–25 fs, the transmitted laser intensities at the depths of 1 nm, 100 nm, and 200 nm are nearly identical to the original Gaussian beam. Hence, in less than 25 fs, the material is transparent to the laser light, which is consistent with the results indicated in Fig. 3, showing the near-zero reflectivity and absorption coefficient. However, after the free electron density becomes comparable to the critical density, the original beam profile is strongly shaped by the generated plasma. For example, at 40 fs, the original laser intensity decreases from about $6.8 \times 10^{13}\,\text{J/cm}^2$ to 4.1×10^{12}, 1.7×10^{12}, and 1.2×10^{12}, respectively, at the depths of 1 nm, 100 nm, and 200 nm. Hence, the laser intensity drastically decreases

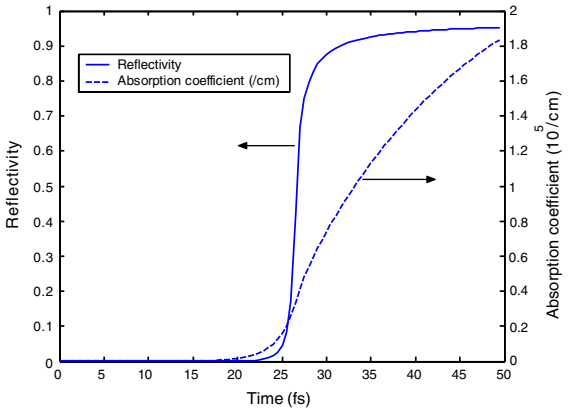

Fig. 3. The reflectivity and absorption coefficient at $r = 0$, $z = 1\,\text{nm}$, $t_p = 50\,\text{fs}$, $F = 5\,\text{J/cm}^2$.

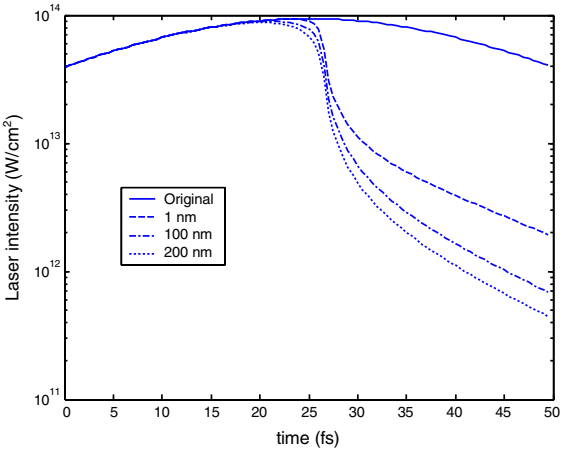

Fig. 4. The laser intensity distribution as a function of time at different depths; $r = 0$, $t_p = 50\,\text{fs}$, $F = 5\,\text{J/cm}^2$.

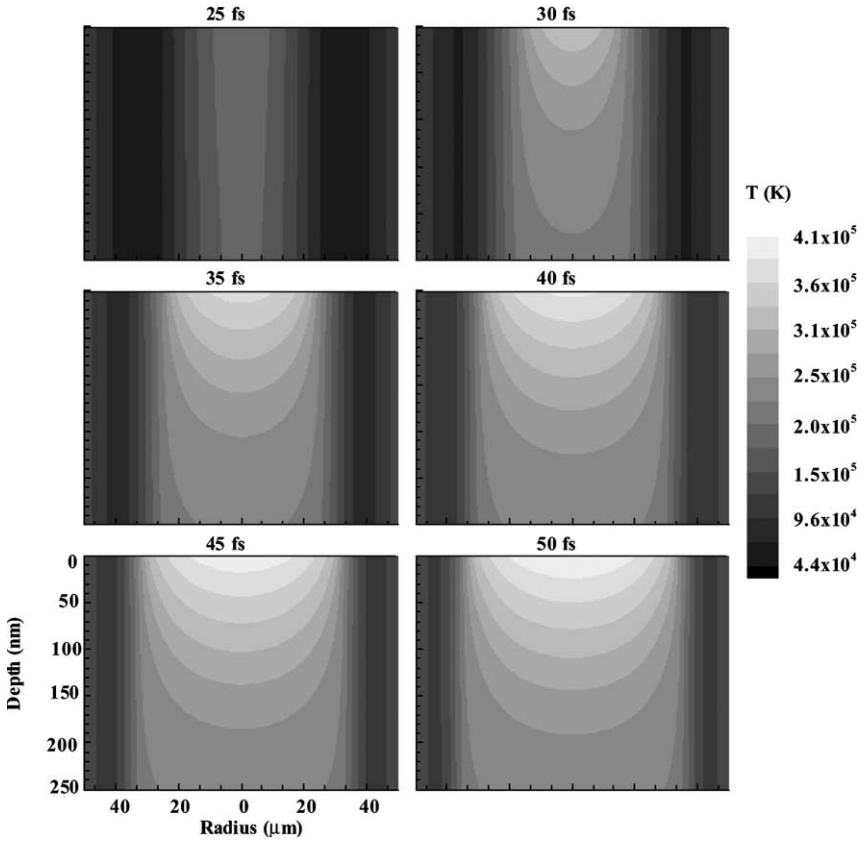

Fig. 5. The free electron temperature distribution at different times; $t_p = 50$ fs, $F = 5$ J/cm^2.

in a few nanometers, which actually indicates a strong skin-effect as discussed previously.

Fig. 5 shows the free electron temperature distribution at different times. It is seen the free electrons in the ablation region are excited to very high temperatures after 25 fs of irradiation. After the critical density is created, although the laser intensity decreases significantly at different depths, as shown in Fig. 4, the electron temperature in the deep of the material, e.g., at 250 nm, still increases significantly from 25 fs and 50 fs. This is caused by the high absorption coefficient, as demonstrated in Fig. 3, and the low heat capacity of free electrons. Note since the electron–phonon interaction is on the order of picoseconds, lattice energy absorption is ignored during the first 50 fs in our calculations.

Fig. 6 shows the free electron density distribution at different times. As expected, the free electron density increases as time increases. The dashed lines trace the locations at which the free electron density is equal to the critical density (1.8×10^{21} cm^{-3}). In each frame, the free electron densities at locations "inside" the dashed line are greater than the critical density, which will be ablated according to our assumption. Hence, the shape of the dashed line represents the shape of the crater at different times. As the critical density has not achieved until 27 fs, as shown in Fig. 2, there is no crater at 25 fs. At 30 fs, the crater shape is still quite Gaussian-like. It is seen in 30–50 fs, the shape of the crater extends more in the radius direction as compared to the depth direction. The final electron density distribution at 50 fs determines the ablation depth and crater shape for 5 J/cm^2 and 50 fs irradiation.

In order to understand the effect of plasma on the laser energy absorption and the resulting ablation crater shape, the laser intensity distributions at different depths and times are plotted in Fig. 7. By comparing Figs. 6 and 7, it is clearly seen that when the critical free electron density is reached, the laser intensity distribution in the material is strongly reshaped. The differences between the original laser intensity profile and the profile at 1 nm are caused mainly by reflection. As shown in Fig. 7, the laser intensity at 1 nm remains nearly constant after 40 fs, which is consistent with the results shown in Fig. 3. On the other hand, the differences of laser intensity at 1 nm and 100 nm are due to the absorption of laser energy by the plasma between these two depths. The strongly reshaped laser intensity profiles lead to a

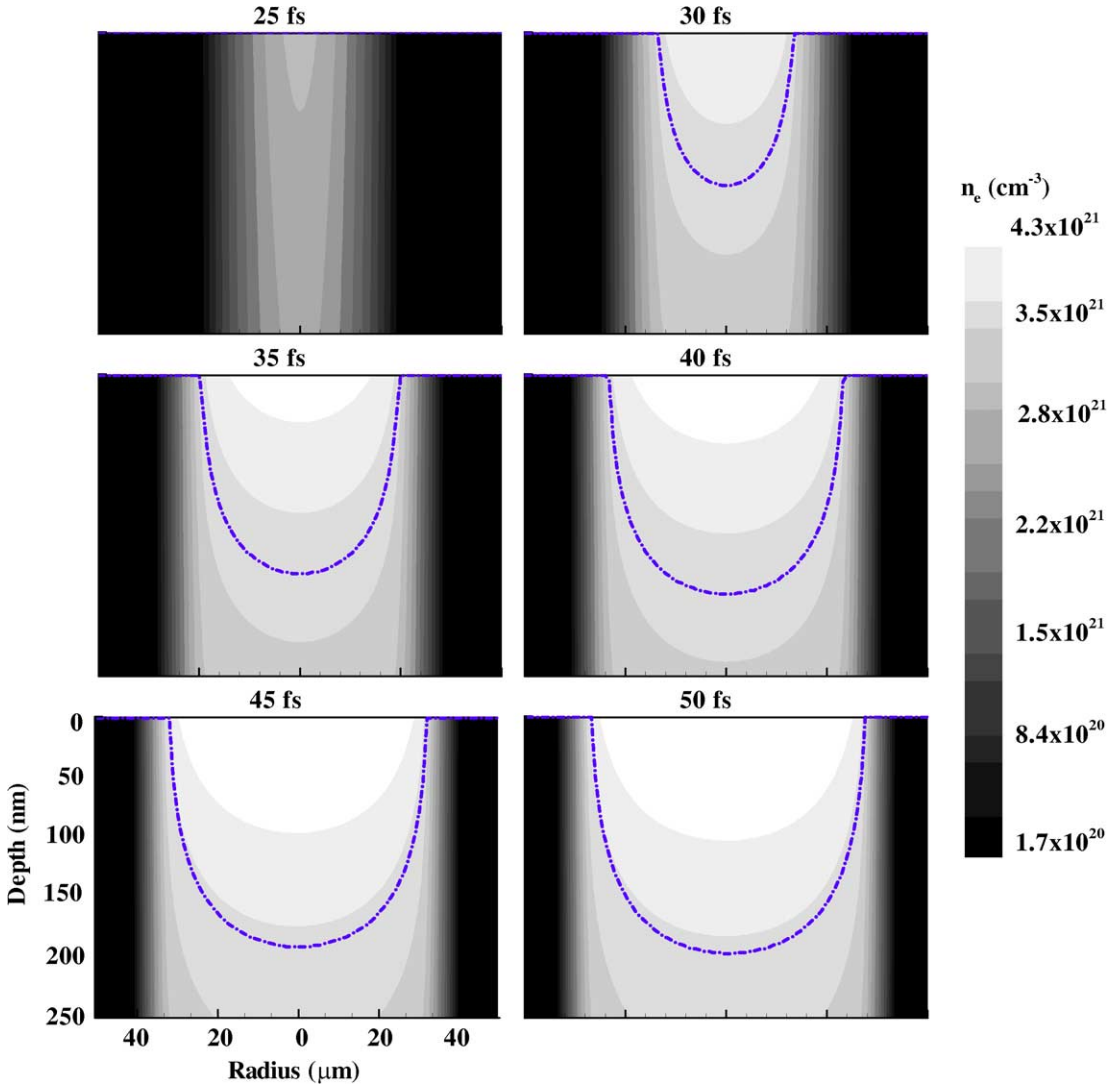

Fig. 6. The free electron density distribution at different times; the dashed lines trace the locations with critical density; $t_p = 50$ fs, $F = 5$ J/cm^2.

nonGaussian shape of crater with a flat-bottom to be discussed next.

The shape of the ablation crater strongly depends on the laser fluences. As shown in Fig. 8, the ablation crater shape is quite Gaussian-like at the laser fluence of 3.3 J/cm^2 by a 780 nm and 50 fs laser pulse. However, the ablation shape at 5 J/cm^2 is rather flat at the bottom as compared to the Gaussian profile. The flat-bottom of the crater at 8 J/cm^2 is even more obvious. Note the Gaussian-like crater shape occurs only when the crater is very small, which can happen at low fluences near the threshold fluence or for a short pulse-duration. The characteristic of the flat-bottom crater shape has been observed experimentally on the femtosecond laser ablation of semiconductors [36]. The flat-bottom crater is caused by the significant changes of the reflectivity and absorption coefficient of the generated plasma, which shapes the laser intensity, as discussed in Fig. 7. Generally, in the femtosecond laser ablation of wide bangap materials, craters with a flat-bottom should be formed, although the degree of flatness depends on the ablation fluence and duration.

Fig. 9(a) shows the change of the ablation depth as a function of fluence. The ablation depth increases drastically from 0 to 195 nm in the fluence range of 3.15–5 J/cm^2 and, then, remains nearly constant. For fused silica used in this study, the predicted ablation depth is in excellent agreement with the experimental result [2],

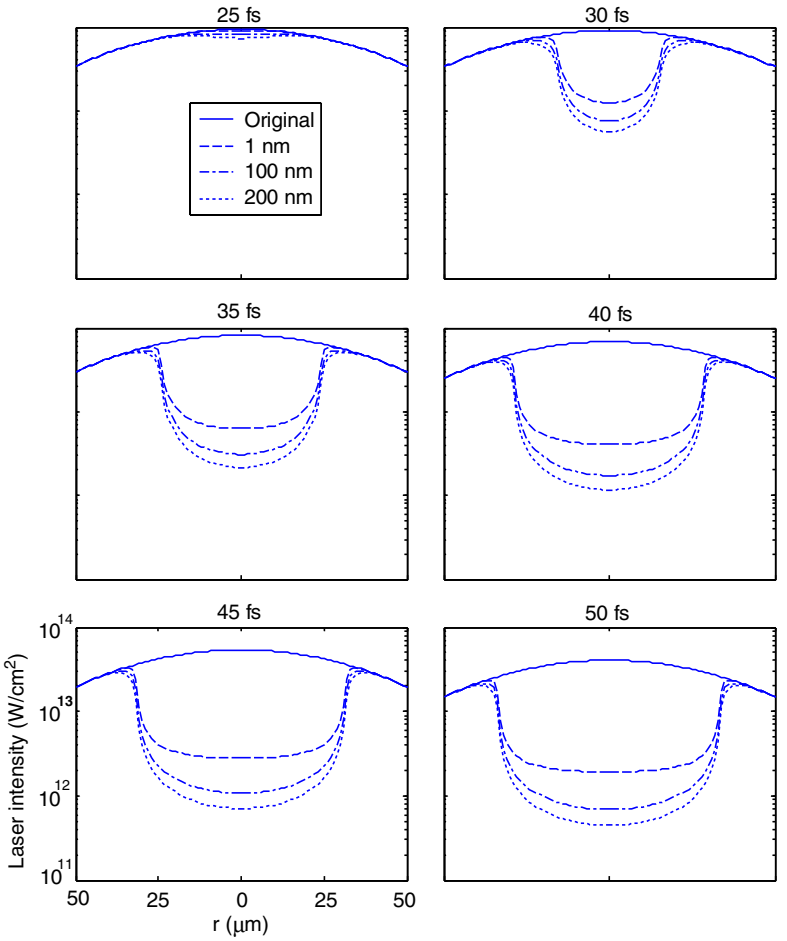

Fig. 7. The laser intensity distribution as a function of radius at different depths and times; $t_p = 50\,\text{fs}$, $F = 5\,\text{J/cm}^2$.

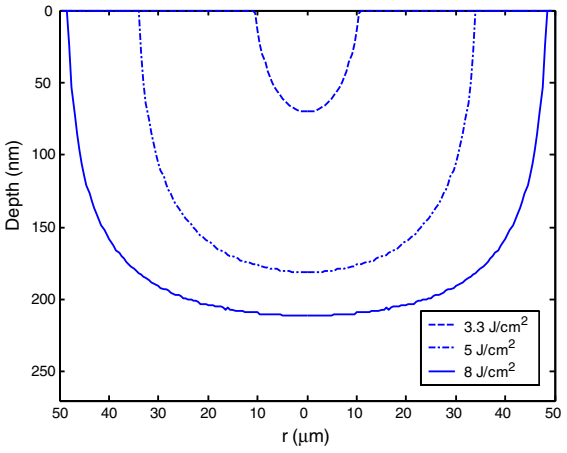

Fig. 8. The ablation crater shape at different fluences; $t_p = 50\,\text{fs}$.

although unfortunately only one data point is available. For the purpose of comparison, the following widely used existing equation is also calculated [37]:

$$d = \left(\frac{1}{\alpha}\right) \ln \frac{F}{F_{\text{th}}} \tag{32}$$

where F_{th} is the threshold fluence. As the absorption coefficient of the material varies significantly as a function of time during the femtosecond laser irradiation, the selection of a "correct" constant absorption coefficient is very challenging. If the absorption coefficient at 25 fs $r = 0$ and $z = 1\,\text{nm}$ under a fluence of $5\,\text{J/cm}^2$ is used, Eq. (32) predicts the curve of ablation depth as shown in Fig. 9(a), which apparently is not consistent with the experimental result. Compared with Eq. (32), our model greatly improves the accuracy in predicting the ablation depth. In the fluence range of 3.15–5 J/cm^2, because the ablation depth is very sensitive to the variation of fluence, it is rather difficult to control the

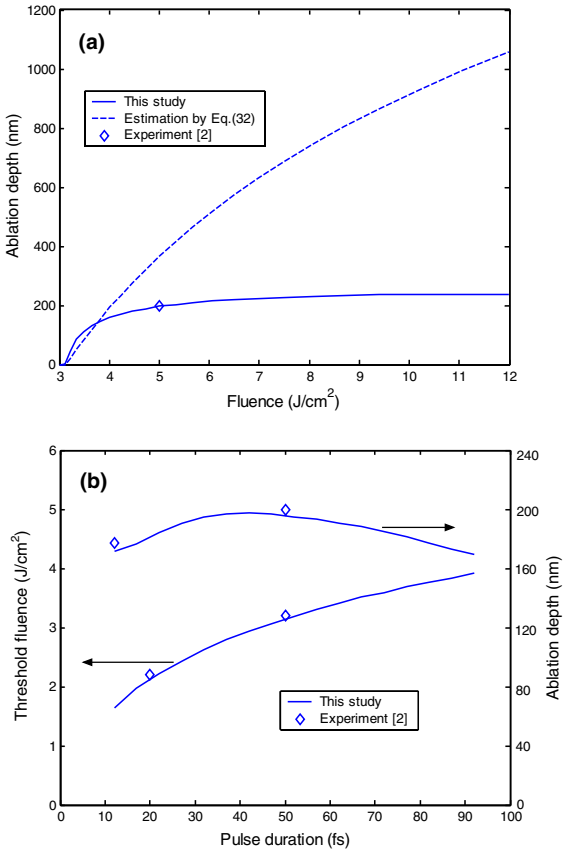

Fig. 9. The threshold fluence and ablation depth: (a) the ablation depth as a function of fluence; $t_p = 50$ fs; (b) the threshold fluence and ablation depth as a function of pulse duration; $F = 5$ J/cm^2 for ablation depth calculations.

accuracy for ablation depth below 200 nm for the 780 nm, 50 fs laser ablation of fused silica. This explains the poor repeatability and controllability in femtosecond laser ablation using fluences slightly above the ablation threshold [38]. On the other hand, from 5 J/cm^2 to 12 J/cm^2, the ablation depth increases very slightly, implying the decrease of photon-cost effectiveness in terms of material removal rate. Hence, in applications it may need to choose an "optimum" fluence in order to achieve ablation quality and high material removal rate for a specific material. The phenomenon of a steep-increase followed by a slow-increase in ablation depth as a function of fluence was also observed in other materials [39,40].

Another important parameter for laser ablation is the pulse duration. Fig. 9(b) shows the threshold fluence and ablation depth as a function of pulse duration. It is seen that the predictions by the present study are in good agreement with the available experimental results. The threshold fluence increases as pulse duration increases which is consistent with our physical intuition. As shown in Fig. 9(b), for a given fluence, 5 J/cm^2, as the pulse duration increases, the ablation depth increases to a maximum (about 195 nm) at about 40 fs and then decreases. When the pulse duration is very short, although the ablation laser intensity (fluence divided by pulse duration) is high, the ablation depth is limited by the very short pulse duration. Hence, as far as the laser intensity is "strong" enough, the ablation depth increases as the pulse duration increases. However, when the pulse duration is increased to some point, the laser intensity becomes "weak" so that the ablation depth decreases as the pulse duration increases. The pulse duration at which the ablation depth reaches the maximum depends on the fluence if other conditions remain unchanged.

4. Conclusions

This paper proposes a plasma model that can predict, for the first time, the crater shape in the femtosecond laser ablation of wide bandgap materials. The model considers the impact ionization and photoionization to calculate the transient distributions of free electron density and free electron temperature. The highly ionized material under the femtosecond laser ablation is treated as plasma, and the plasma model for metals and doped semiconductors is modified for wide bangap materials to investigate the time and space dependence of optical properties and laser intensity. Quantum treatment is employed to determine the free electron specific heat, temperature, and relaxation time. The ablation threshold fluence and depth predicted by the proposed model are in excellent agreement with the experimental measurements for fused silica. The following conclusions can be drawn from the present study: (1) the strong temporal and spatial dependent optical properties of the highly ionized material are proved to play a critical role in shaping the laser intensity profile in the material; (2) the experimentally observed flat-bottom crater is predicted by the proposed model which is attributed to the variations of optical properties of the dense plasma; (3) it is difficult to achieve high repeatability of ablation at fluences slightly higher than the ablation threshold fluence. Although high repeatability may be achieved for fluences much higher than the threshold fluence, the photon-cost effectiveness in terms of material removal rate decreases; (4) depending upon fluences, as the pulse duration increases, the ablation depth increases, to a peak value, and then decreases.

Acknowledgement

This work was partially supported by the National Science Foundation under Grants No. 0116158 and No. 0423233.

References

[1] K. Kawamura, T. Ogawa, N. Sarukura, M. Hirano, H. Hosono, Fabrication of surface relief gratings on transparent dielectric materials by two-beam holographic method using infrared femtosecond laser pulses, Appl. Phys. B 71 (1) (2000) 119–121.

[2] M. Lenzner, J. Krüger, S. Sartania, Z. Cheng, C. Spielmann, G. Mourou, W. Kautek, F. Krausz, Femtosecond optical breakdown in dielectrics, Phys. Rev. Lett. 80 (1998) 4076–4079.

[3] A. Kaiser, B. Rethfeld, M. Vicanek, G. Simon, Microscopic processes in dielectrics under irradiation by subpicosecond laser pulses, Phys. Rev. B 61 (2000) 11437–11450.

[4] F. Quéré, S. Guizard, P. Martin, Time-resolved study of laser-induced breakdown in dielectrics, Europhys. Lett. 56 (1) (2001) 138–144.

[5] S.C. Jones, P. Braunlich, R.T. Casper, X.A. Shen, P. Kelly, Recent progress on laser-induced modifications and intrinsic bulk damage of wide-gap optical materials, Opt. Eng. 28 (1989) 1039–1068.

[6] D.V. Linde, H. Schüler, Breakdown threshold and plasma formation in femtosecond laser-solid interaction, J. Opt. Soc. Am. B 13 (1996) 216–223.

[7] X. Liu, D. Du, G. Mourou, Laser ablation and micromachining with ultrashort laser pulse, IEEE J. Quant. Elect. 33 (1997) 1706–1716.

[8] F. Ladieu, P. Martin, S. Guizard, Measuring thermal effects in femtosecond laser-induced breakdown of dielectrics, Appl. Phys. Lett. 81 (2002) 957–959.

[9] J.C. Diels, W. Rudolph, Ultrashort Laser Pulse Phenomena, Academic Press, 1996.

[10] P. Gibbon, E. Forster, Short-pulse laser-plasma interactions, Plasma Phys. Control Fus. 38 (1996) 769–793.

[11] L. Jiang, H.L. Tsai. Challenges in microscopic energy transport during femtosecond laser ablation of wide bandgap materials, J. Laser Appl. 2003 (in review).

[12] C. Cornaggia, in: J. Posthumus (Ed.), Molecules and Clusters in Intense Laser Fields, Cambridge University Press, Cambridge, UK, 2001.

[13] H.P. Cheng, J.D. Gillaspy, Nanoscale modification of silicon surfaces via Coulomb explosion, Phys. Rev. B 55 (1997) 2628–2636.

[14] R. Stoian, D. Ashkenasi, A. Rosenfeld, E.E.B. Campbell, Coulomb explosion in ultrashort pulsed laser ablation of Al_2O_3, Phys. Rev. B 62 (2000) 13167–13173.

[15] V.P. Krainov, A.S. Roshchupkin, Dynamics of the Coulomb explosion of large hydrogen iodide clusters irradiated by superintense ultrashort laser pulses, Phys. Rev. A 64 (2001) 063204–063208.

[16] L. Jiang, H.L. Tsai, Femtosecond laser ablation: challenges and opportunities, in: Proceedings of NSF Workshop on Research Needs in Thermal, Aspects of Material Removal, Stillwater, OK, 2003.

[17] P.P. Pronko, P. VanRompay, A. Horvath, C.F. Loesel, T. Juhasz, X. Liu, G. Mourou, Avalanche ionization and dielectric breakdown in silicon with ultrafast laser pulses, Phys. Rev. B 58 (1998) 2387–2390.

[18] A. Tien, S. Backus, H. Kapteyn, M. Murnane, G. Mourou, Short-pulse laser damage in transparent materials as a function of pulse duration, Phys. Rev. Lett. 82 (1999) 3883–3886.

[19] B.C. Stuart, M.D. Feit, A.M. Rubenchik, B.W. Shore, M.D. Perry, Laser-induced damage in dielectrics with nanosecond to subpicosecond pulses, Phys. Rev. Lett. 74 (1995) 2248–2251.

[20] B.C. Stuart, M.D. Feit, S. Herman, A.M. Rubenchik, B.W. Shore, M.D. Perry, Nanosecond-to-femtosecond laser-induced breakdown in dielectrics, Phys. Rev. B 53 (1996) 1749–1761.

[21] M.D. Perry, B.C. Stuart, P.S. Banks, M.D. Feit, V. Yanovsky, A.M. Rubenchik, Ultrashort-pulse laser machining of dielectric materials, J. Appl. Phys. 85 (1999) 6803–6810.

[22] P.P. Pronko, S.K. Dutta, D. Du, R.K. Singh, Thermophysical effects in laser processing of materials with picosecond and femtosecond pulses, J. App. Phys. 78 (10) (1995) 6233–6240.

[23] M.D. Shirk, P.A. Molian, A review of ultrashort pulsed laser ablation of materials, J. Laser Appl. 10 (1998) 18–28.

[24] E.G. Gamaly, A.V. Rode, B. Luther-Davies, V.T. Tikhonchuk, Ablation of solids by femtosecond lasers: ablation mechanism and ablation thresholds for metals and dielectrics, Phys. Plas. 9 (2002) 949–957.

[25] X. Xu, G. Chen, K.H. Song, Experimental and numerical investigation of heat transfer and phase change phenomena during excimer laser interaction with nickel, Int. J. Heat Mass Transfer 42 (1999) 1371–1382.

[26] D. Du, X. Liu, G. Korn, J. Squier, G. Mourou, Laser-induced breakdown by impact ionization in SiO_2 with pulse widths from 7 ns to 150 fs, Appl. Phys. Lett. 64 (1994) 3071–3074.

[27] B. Rethfeld, A. Kaiser, M. Vicanek, G. Simon, Ultrafast dynamics of nonequilibrium electrons in metals under femtosecond laser irradiation, Phys. Rev. B 65 (2002) 214303–214313.

[28] M. Fox, Optical Properties of Solids, Oxford University Press, Oxford, 2001.

[29] E.M. Lifshitz, L.P. Pitaevskii, Physical Kinetics, Pergamon, Oxford, 1981.

[30] W.L. Kruer, The Physics of Laser Plasma Interaction, Addison Wesley, New York, 1987.

[31] K. Eidmann, J. Meyer-ter-Vehn, T. Schlegel, S. Hüller, Hydrodynamic simulation of subpicosecond laser interaction with solid-density matter, Phys. Rev. E 62 (2000) 1202–1214.

[32] Y.T. Lee, R.M. More, An electron conductivity model for dense plasma, Phys. Fluids 27 (5) (1984) 1273–1286.

[33] N.W. Ashcroft, N.D. Mermin, Solid State Physics, Holt, Rinehart, and Winston, 1976.

[34] J.W. Rohlf, Modern Physics from α to Z^0, Wiley, New York, 1994.

[35] L. Jiang, N. George, H.L. Tsai, Prediction of damage threshold fluences for metal films by an ultrashort laser pulse, in: Proceedings of the 5th International Symposium on Laser Precision Micromachining, Nara, Japan, 2004.

[36] A.S. Zakharov, M.V. Volkov, I.P. Gurov, V.V. Temnov, K. Sokolovski-Tinten, D. von der Linde, Interferometric diagnostics of ablation craters formed by femtosecond laser pulses, J. Optical Tech. 69 (7) (2002) 478–482.

[37] J. Krüger, W. Kautek, The femtosecond pulse laser: a new tool for micromaching, Laser Phys. 9 (1999) 30–40.
[38] B.N. Chichkov, A. Ostendorf, F. Korte, S. Nolte, Femtosecond laser ablation and nanostructuring, in: Proceedings of ICALEO 2001, Jacksonville, FL, October 2001.
[39] M. Lapczyna, K.P. Chen, P.R. Herman, H.W. Tan, R.S. Marjoribanks, Ultra-high repetition rate (133 MHz) laser ablation of aluminum with 1.2-ps pulses, Appl. Phys. A 69 (Suppl) (1999) S883–S886.
[40] K. Furusawa, K. Takahashi, S.H. Cho, H. Kumagai, K. Midorikawa, M. Obara, Femtosecond laser micromachining of TiO_2 crystal surface for robust optical catalyst, J. Appl. Phys. 87 (2000) 1604–1609.